Mapping the molecular landscape of the living brain: integrating spatial transcriptomics and qMRI

Melissa Grant-Peters[1,2,*], George E C Thomas[3,*], Angelika Zarkali[3], Ivelina Dobreva[3], Rimona Weil[3,4,5,*], Mina Ryten[1,2,6,*,+]

1. UK Dementia Research Institute at The University of Cambridge, Cambridge, CB2 0AH, UK
2. Department of Clinical Neurosciences, School of Clinical Medicine, The University of Cambridge, Cambridge, CB2 0QQ, UK
3. Dementia Research Centre, University College London, London, WC1N 3AR, UK
4. Wellcome Centre for Human Neuroimaging, University College London, London, WC1N 3AR, UK
5. Movement Disorders Centre, National Hospital for Neurology and Neurosurgery, London, WC1N 3AR, UK
6. Department of Medical Genetics, NIHR Cambridge Biomedical Research Centre, University of Cambridge, Cambridge, UK

* These authors contributed equally

+ corresponding author

Abstract

Disease modifying therapies targeting specific molecular disease processes are becoming increasingly available for neurodegenerative disorders. However, profiling molecular features of neurodegeneration in living patients is challenging due to limited accessibility to brain tissue. In this work, we demonstrate that we can infer cell type presence and expression of molecular pathways at a sub-cortical level from ultra-high resolution 7T quantitative MRI by leveraging in-depth molecular characterisation of spatial transcriptomics (ST) data. We demonstrate the applicability of our approach to characterising disease by predicting molecular features in a Parkinson's disease cohort. From qMRI data we predict disruption to the distribution of oligodendrocytes in the grey-matter cortex consistent with altered oligodendrocyte maturation. Our method contributes to advancing precision medicine in neurodegeneration, with promising attributes including cost-effectiveness, tolerability and clinical accessibility, with potential for clinical impact.

Introduction

Drugs designed to target specific molecular features, such as genetic variants, are considerably more likely to succeed than non-targeted therapies. Consequently, stratifying patients based on molecular features has transformed drug development and disease treatment across disease areas, particularly in cancer (1,2) and, more recently, in autoimmunity (3). In contrast, applying molecular classification to neurodegeneration is especially challenging due to the inaccessibility of brain samples and ethical implications of sampling. This has largely restricted patient stratification to genotype-specific treatments which are not applicable to most complex diseases. With the recent emergence of disease-modifying therapies for conditions like Alzheimer's disease (4) and amyotrophic lateral sclerosis (5), the need for precision medicine approaches in neurology is becoming increasingly urgent to guide both clinical trial design and therapeutic decision-making.

Meeting this need requires a precision medicine framework that is both patient-centred and compatible with existing clinical infrastructure. Such an approach must ensure tolerability (favouring non-invasive methods over biopsies or high-risk procedures), enable simultaneous profiling of multiple molecular features to reduce cost and procedural burden, and maximise the utility of resources already in place. Strategies that fail to meet these criteria can struggle to achieve clinical translation; for example, lecanemab for Alzheimer's disease (4) requires early-stage confirmation via PET imaging, but the limited availability of PET infrastructure has constrained its population-level impact.

Magnetic resonance imaging (MRI) offers a way forward, as it satisfies many of these requirements by providing a non-invasive, widely accessible, and clinically established platform. Moreover, it can be further developed to capture molecular as well as structural features of disease. For example, in multiple sclerosis, MRI has become indispensable for diagnosis, disease monitoring, and treatment decisions, illustrating how imaging can successfully anchor a precision medicine framework in neurology. MRI has also proven valuable for assessing neurodegenerative disorders, with structural MRI yielding spatially resolved insights into disease processes by tracking anatomical changes across affected brain regions. In many neurodegenerative conditions, where progression follows a region-specific trajectory, these spatial data have the potential to inform both disease staging and longitudinal monitoring. Structural changes emerge only after profound and irreversible cellular damage, making it essential to develop imaging strategies that reveal molecular alterations earlier in the disease course (**Fig 1A**).

Quantitative MRI (qMRI) directly addresses this need by extending MRI to capture molecular-level features through advanced imaging sequences. It is increasingly gaining traction, with techniques such as multi-parameter mapping (MPM) (6) enabling the extraction of a wide range of continuous, quantitative variables across the whole brain and cortex. These provide insight into tissue microstructure and potentially capture dynamic changes across the disease course, from prodromal to late stages (6–9). In contrast with PET imaging, qMRI is more widely available, and the deployment of novel imaging sequences is significantly faster than the

deployment of novel radiotracers, which requires several additional steps including regulatory approval (10,11). Despite this, qMRI, including MPM, remains relatively underutilized clinically (12) and is typically employed as an adjunct to conventional structural imaging.

A major barrier to the clinical translation of qMRI is the limited interpretability of its metrics (13,14), which reflect a complex mixture of cellular and molecular sources (15,16), some of which have yet to be explicitly validated. At the same time, molecular profiling technologies have advanced dramatically. Spatial transcriptomics (ST) now enables untargeted, spatially resolved quantification of tens of thousands of RNA species from a single tissue section, offering unprecedented molecular context, but is largely confined to the postmortem brain. Recent improvements in ultra-high-field MRI (7T, 11T) provide sufficient spatial resolution to integrate qMRI with ST, aligning microstructural imaging with molecular data. This convergence creates a timely opportunity to resolve the biological bases of qMRI metrics and unlock their potential for precision medicine in neurology (**Fig 1B**).

In this work, we use postmortem spatial transcriptomics data to model the inference of molecular insights from qMRI data in living brains on a subcortical level. We demonstrate that molecular pathways and cell type presence have significant correlative relationships with qMRI metrics, and that disruptions to these metrics in disease are predictable with qMRI data. Our approach has especially high potential for disease staging and patient stratification for clinical trials

Results

Defining common cortical spatial domains in qMRI and spatial transcriptomics
Our live imaging cohort consisted of 21 healthy controls (age = 67.7 ± 7.96, 10/21 females). Multi-parameter mapping (MPM) sequences were acquired on a 7T MRI system at 0.6mm isometric resolution. From these, we generated quantitative maps of magnetic susceptibility (QSM), proton density (PrD), longitudinal relaxation rate (R1), transverse relaxation rate (R2*), and magnetization transfer saturation (MTsat). Each of these metrics is sensitive to differing microstructural features in the tissue. In brief, QSM is primarily sensitive to paramagnetic iron and diamagnetic myelin (which have opposing influences) (17), R1 to myelin-related macromolecular content (and secondarily to iron and tissue water fraction) (18); R2* to iron and to a lesser extent myelin (19); MTsat to macromolecular structures including myelin (20); and proton density to tissue water fraction (21). For the ST data, we leveraged publicly available dorsolateral prefrontal cortex data generated using the 10x Visium technology (22). This dataset included 30 brain samples from 10 individuals without a neurological condition at the time of death (age = 49.51, 4/10 females).

Due to availability of high quality spatial transcriptomics data, we focused this work on the human dorsolateral prefrontal cortex (DLPFC, Broadmann area 46). Moreover, this is a well defined area both for dissection and selection on MRI which is involved in several neurological conditions, including neurodegenerative and neuropsychiatric disorders (23–26). Firstly, we ensured that the DLPFC from both methods was partitioned into three regions, namely anterior,

middle and posterior DLPFC, with the pathologist responsible for dissection of postmortem brains guiding subsetting of the MRI data to match. Secondly, we partitioned the grey matter cortex into 4 spatial domains, which was the largest number of layer partitions allowed by the spatial resolution of the MRI imaging (**Fig 1C,D**). For MRI data, the DLPFC was defined using structural MP2RAGE images brought into MPM space. Four equivolume spatial domains were subsequently defined within the three DLPFC subregions. For ST data, we used a molecularly- and spatially-informed partitioning, with similar area across the spatial domains but preserving the inherent cellular architecture of the DLPFC cortex. We therefore defined 12 common regions of interest (ROIs) across four spatial domains and three DLPFC subregions for both ST and MRI data. In this way, we generated a spatial integration framework, which could be used to investigate the relationships between qMRI and ST metrics (**Fig 1E**).

qMRI metrics correlate with lipid, myelin and inflammation pathway scores

We first investigated the extent to which qMRI metrics were associated with biological processes across spatial domains (**Fig 2A**). We found that qMRI metrics varied approximately linearly across cortical spatial domains, similarly to previous reports (27,28). Given the relatively limited spatial sampling of the dataset and the absence of subject-level matching between ST and qMRI data, we opted for linear modelling as a conservative, low complexity strategy.

In order to explore the pathway-qMRI relationship, we chose to leverage gene ontology biological process pathways, which collate lists of genes involved in specific pathways (**Fig 2B**). This allowed us to score the ST spatial domains based on specific pathways, and to know whether this collection of genes was more or less expressed relative to background genes.

We chose to focus this investigation on four pathway categories: lipid, myelin, iron and inflammation. The first three due to the expectation that qMRI metrics should capture metrics associated with these pathways. We opted to include inflammation pathways as an exploratory option, due to the clinical value there would be in inferring inflammation from qMRI metrics for diagnosis and prognosis. All pathways including these keywords were selected as well as all their offspring pathways. We then filtered these pathways based on our confidence to capture them on a molecular level, where all pathways with 5 genes or less were excluded and all pathways where less than 50% of the genes were captured in our spatial transcriptomics dataset were also excluded. Finally, we calculated the median pathway score in each transcriptomic spatial domain. We similarly extracted median qMRI values from the 12 ROIs.

Lipid pathways had the most significant correlations with qMRI metrics, where a pathway was considered significant if the $R^2 > 0.85$ and FDR-adjusted pvalue<0.05 (**Fig 2C**). A total of 14 pathways had positive correlations with qMRI matrics, of which one related to inflammation (inflammatory response, correlation with R2*), one related to myelin (regulation of oligodendrocyte differentiation, correlation with Prd, R2* and MTsat) and 12 related to lipid metabolism. PrD and R2* were the qMRI metrics with the highest numbers of significant correlations with specific pathway expression. These pathways related to various processes including splicing (U2-type catalytic step 2 spliceosome, paraspeckles), lipid metabolism (fatty acid elongation, galactosylceramide biosynthetic process, phosphatidylinositol-3-phosphate

biosynthetic process, fatty acid metabolic process), transport and binding (phosphatidylserine floppase activity, release of sequestered calcium ion into cytosol by sarcoplasmic reticulum, phospholipid-translocating ATPase complex, glycolipid binding), and complex pathways such as response to vitamin D (**Fig 2D**). Associations between these 14 pathways and all qMRI metrics can be seen in **SupFig 1**.

Glial cell counts significantly correlate with qMRI metrics

Having found strong associations between qMRI and pathway scores, we next hypothesised that qMRI metrics would be associated with cell counts (**Fig 3A**). The central nervous system contains cell types which are rich in lipids and iron, both of which are large sources of qMRI signal. Therefore, we wanted to explicitly evaluate whether qMRI metrics might reflect the number of each given cell type.

The 10x Visium technology used for the ST data does not generate single cell level spatially resolved data, but rather each spatial unit is estimated to contain 3-6 cells. Therefore, in order to assess the relationship between cell type occurrence and qMRI metrics, we first needed to predict which cell types were most likely to be in each given spatial unit (spot). To do this, we used the cell2location deconvolution method. This approach used paired single nuclear RNA sequencing data to predict the cell types most likely to be present in a given spatial unit. We considered the top 3 cells with highest scores to be present, since these were the ones we had highest confidence for. This provided us with cell type counts in each spatial domain across all samples. This, in turn, was summarised as the median count of each cell type in each of the 12 ROIs. We extracted median qMRI values as before.

We found that the cell type with most significant relationships with qMRI metrics was oligodendrocytes, which had significant positive correlations with all qMRI metrics (**Fig 3B,C**,$0.68<R^2<0.80$, $2.1e10^{-3}$ < FDR-adjusted p-value < $5.1e10^{-3}$). Since oligodendrocytes are the cell type which has both the highest myelin and iron content, strong correlations with qMRI metrics are to be expected. By contrast, microglia and astrocytes had significant negative correlations with all metrics except QSM, whilst oligodendrocyte progenitor cells (OPCs) had the lowest number of significant correlations, having significant relationships with MTsat, PrD and R1. In summary, we expect that qMRI metrics are capturing cell type specific information, especially for mature oligodendrocytes.

qMRI metrics can predict molecular pathways

Observing that many GO pathways exhibited significant associations with at least three qMRI metrics, we hypothesised that a multivariate qMRI model could be used to predict GO pathway score. Therefore, we modelled each pathway score as a linear combination of qMRI metrics. Predictive performance was assessed across 12 ROIs using leave-one-out cross validation (LOOCV), since this provided a robust framework for the number of samples available for this study. In summary, one ROI was iteratively withheld, while the multivariate model was fitted across remaining ROIs, and used to predict the pathway score. We found that for all of these pathways, the scores could be reliably predicted, with strong and highly significant correlations

between predicted and actual values ($0.55<R^2<0.92$, $1.3 \times 10^{-5}<$ FDR-adjusted p-value $< 5.8 \times 10^{-3}$, **Fig 4A**).

qMRI indicates disruption to lipid pathways in Parkinson's disease

To assess the translatability of our findings, we wanted to predict cell counts in a clinical dataset (**Fig 4B**). We utilised 7T qMRI data from 31 people with Parkinson's disease (PD), acquired with the same protocol as for healthy controls, and extracted qMRI metrics from the 12 ROIs using identical processing steps. First, we performed a head-to-head comparison of control vs PD qMRI metrics across the spatial domains. We found a significant decrease in MTsat levels in PD specific to SpD1 (FDR-adjusted p-value = 1.2×10^{-6}, **Fig 4C**), along with a decrease in R1 in the same spatial domain (FDR-adjusted p-value = 3.6×10^{-2}, **Fig 4D**). Comparison between Parkinson's and controls for all other qMRI metrics can be seen in **SupFig 2**.

The control pathway analysis informed us that MTsat and R1 only significantly correlated simultaneously in lipid-associated pathways, such as paraspeckles, fatty acid metabolic process, and response to vitamin D. We first attempted to predict the pathway scores using the prediction model. Our comparison of predicted pathway scores in PD and real pathway scores in controls did not significantly differ, suggesting a lipid pathway with a more complex relationship with qMRI metrics might be affected.

qMRI metrics can predict cell type counts

We next aimed to verify whether cell type counts could be predicted using a combination of qMRI metrics, as for GO pathways. We used the same LOOCV approach across the 12 ROIs as described for GO pathways, and found that the predicted cell counts significantly correlated with actual counts for all cell types, with microglia having the strongest correlation ($R^2 = 0.79$, FDR-adjusted p-value = 3.3×10^{-3}, **Fig 5A**). Upon visual inspection, we found that the correlations for microglia, astrocytes and OPCs were largely reliant on the SpD1 scores, with low variation in the cell counts across SpD2-4. Therefore, to assess robustness, we calculated Cook's distance, and found that the correlations were not sensitive to the removal of any one of the ROIs (**SupFig 3**). Nevertheless, we had highest confidence in the robustness of the prediction of oligodendrocyte counts ($R^2 = 0.40$, FDR-adjusted p-value = $3.3e10^{-2}$), since all spatial domains contributed to the correlation relationship.

qMRI metrics predict changes in oligodendrocyte populations in Parkinson's disease

In order to predict cell counts in PD, we applied the parameters developed in LOOCV to the PD qMRI data. This provided us with a prediction of cell counts in PD for each ROI. To verify whether these predicted cell type counts differed from controls, we correlated predicted PD counts with the median real counts from controls. We hypothesised that a high correlation would indicate that there were no significant changes in cell type proportions across the cortex in PD, whereas a poor fit would indicate a significant change in cell type numbers or properties in PD.

We found that for astrocytes, microglia and OPCs the predicted cell counts in PD had significant correlations with the real control cell counts ($0.468<R^2<0.811$, $1.876 \times 10^{-2}<$ FDR-adjusted p-value $< 2.578 \times 10^{-4}$, **Fig 5B**). However, when the correlation analysis was performed for

oligodendrocytes, we noted two significant features: first, that the prediction included negative cell counts and secondly, that there was no longer a significant correlation between the predicted cell counts in PD and the real counts in controls (R^2 = 0.137, FDR-adjusted p-value = 2.359 $x10^{-1}$). This suggested that in the context of disease there were significant changes to the oligodendrocyte population. Namely, that there was a lower oligodendrocyte population in PD than in the controls used to build the model, and that there was variation in the spatial distribution of oligodendrocytes across the cortical grey matter.

These findings support the hypothesis that qMRI data can be used to detect spatial domain specific molecular and cellular changes to lipid metabolism and oligodendrocyte populations, which provide novel insight into neurological disease in live patients.

Discussion

With the emergence of disease modifying therapies for neurodegenerative disorders, new tools are needed to stratify patients non-invasively. In this study we explore the untapped potential of spatial transcriptomics and qMRI to infer cellular and molecular features of the living brain. To our knowledge, this is the first time a study has integrated MRI and spatial transcriptomics at subcortical resolution. While previous studies have quantified the relationship between gene expression and MRI, this was done in a brain region-specific manner. In contrast, our approach focused on microstructure allowing clearer links between specific cytoarchitectural features and cortical organisation of the brain. Profiling this level of resolution is especially relevant in neurodegeneration, as cell-type specific analyses have revealed selectively vulnerable cell types in specific neurodegenerative disorders, particularly among excitatory neurons resident to specific cortical layers, such as CUX2 neurons in multiple sclerosis (29) and RORB neurons in Parkinson's disease (30). Moreover, the role of more dynamic and mobile cell types, specifically glia, are increasingly implicated in neurological diseases, including neurodegenerative processes. Therefore, we employed computational algorithms to quantify qMRI changes from deep to surface grey matter cortex, and then went on to study their relationship with glia.

We first assessed the simplest type of predictive relationships between qMRI and ST data, that is, significant linear relationships through correlative analysis of individual variables. We detected multiple molecular pathways with significant strong correlations with qMRI metrics, including ones associated with inflammation, myelin and lipid metabolism. Lipid metabolism had the most significant relationships with qMRI metrics, suggesting this metric to be particularly well captured by qMRI. We also detected multiple significant correlations between glial cell counts and qMRI metrics; oligodendrocytes in particular had significant correlations across all qMRI metrics, suggesting qMRI might have predictive potential for estimating glial cellular populations. We went on to demonstrate that from qMRI metrics we could significantly predict molecular pathways and cell counts. Across all cell types, prediction of oligodendrocytes was especially robust.

We demonstrated the applicability of these models in the context of disease by employing them in PD. The model predicted significant changes to the oligodendrocyte population in PD, both in

number and in spatial distribution. Observing spatial-domain specific changes to the oligodendrocyte population is consistent with known oligodendrocyte biology. Specifically, white matter OPCs have faster proliferation, more dynamic migration and higher sensitivity to inflammatory signals. In contrast, grey matter OPCs have slower differentiation into mature oligodendrocytes (31). These features are consistent with the fact that the cortical spatial domains would respond to oligodendrocyte loss at different rates, creating a variable gradient of oligodendrocytes in disease.

A limitation of this study is the relatively small cohorts used for qMRI and ST data collection. Furthermore, our prediction model was based entirely on control data. We expect that through the use of larger cohorts including disease data the models would be more complex, robust and interpretable. Nevertheless, we have demonstrated that, through ST-informed analysis of qMRI data, we were able to detect subcortical variation in specific cell types and pathways. Jointly, this analysis provided novel insight into disease processes in the living brains of individuals with neurological disease.

Our-proof-of-concept study shows a cost-effective, highly tolerable and scalable approach to precision medicine which allows the profiling of molecular disease features in living patients. We believe this work paves the way for accessible computational tools with transformative potential for neurodegeneration research and clinical practice.

Acknowledgments

MGP is supported by the MS society (project number RRAG/480). AZ is supported by an Alzheimer's Research UK Clinical Research Fellowship (2021B-001). RW is supported by a Wellcome Career Development Award (225263/Z/22/Z). This work is supported by the UK Dementia Research Institute (award number UK DRI-2206) through UK DRI Ltd, principally funded by the Medical Research Council (MR).

Competing Interests

RW has received speaking and writing honoraria respectively from GE Healthcare and Britannia, and consultancy fees from Therakind, and is local PI for an EIP neflamapimod trial.

Materials and Methods

MRI participants

32 people with PD within 10 years of diagnosis were recruited to our London centre. Inclusion criteria were clinically diagnosed, early to mid-stage PD (Queen Square Brain Bank Criteria) aged 50 to 80 years. Exclusion criteria were confounding neurological or psychiatric disorders, dementia and metallic implants considered unsafe for MRI. Participants continued their usual therapy (including levodopa) for all assessments. No patients were taking cholinesterase

inhibitors. In addition, we recruited 21 age-matched controls from sources including unaffected patient spouses. All participants gave written informed consent. After MRI quality control (conducted blinded to patient group), five PD participants were excluded. Thus, 27 participants with PD (age 66.2±7.24, mean±SD; 6 female) and 21 healthy controls (age 67.7±7.96, mean±SD; 10 female) were included in the current study (see Table 1 for demographics).

MRI acquisition

All participants underwent multiparametric mapping (MPM) as well as magnetization-prepared 3D rapid multishot gradient-echo (MP2RAGE) anatomical imaging on a 7T whole-body MRI system (Magnetom 7T, Siemens Healthineers, Erlangen, Germany) equipped with a 1-channel transmit/32-channel radio-frequency receive head coil (Nova Medical, Wilmington, MA). The MPM protocol consisted of three multi-echo fast low angle shot (FLASH) scans with T1, proton density and magnetization-transfer weighting (T1w, PDw and MTw) that had 0.6mm isotropic resolution, a readout bandwidth of 469Hz/pixel and an acquisition time of 9mins 10secs each. The T1w scan was acquired with a flip angle (FA) of 24°, six evenly spaced echoes of alternating polarity between 2.3 and 14.2ms and a TR of 19.5ms; the PDw scan with an FA of 6°, six evenly spaced echoes of alternating polarity between 2.2 and 14.1ms and a TR 19.5ms; and the MTw scan with an FA of 6°, four evenly spaced echoes of alternating polarity between 2.2 and 9.34ms, a TR 19.5ms and an MT contrast pulse angle of 180°. Before each sequence, a low resolution 4mm isotropic image with the same acquisition parameters was acquired to measure the receive field (RF) sensitivity (32). An estimate of the B1+ transmit field was calculated at the time of scanning using a 3D Bloch-Siegert based approach (33). MP2RAGE scans were acquired with the following parameters: 0.7mm isotropic resolution, TR=5000ms, TE=2.54ms, TI1=900ms, TI2=2750ms, FA1=5°, FA2=3°, readout bandwidth=240Hz/pixel and an acquisition time of 8mins 42secs.

qMRI map creation

Quantitative MPM maps of the longitudinal relaxation rate (R1), transverse relaxation rate (R2*) and magnetization transfer saturation (MTsat) were calculated using the hMRI toolbox (34) for Statistical Parametric Mapping (SPM) in MATLAB. All acquisitions were coregistered to their corresponding PDw scan. R1 maps were estimated from the PDw and T1w data using approximations of the signal equations for small repetition time (35), (36). R2* maps were derived from the exponential TE dependence of the PDw and T1w signal using the ESTATICS model and weighted least squares fitting (37). MTsat maps were calculated from the R1 map and MTw sequence using the small excitation flip angle approximation (35). RF sensitivity bias correction was completed using the acquired per-contrast sensitivity maps and B1+ bias correction was completed using the pre-calculated map from the Bloch-Siegert acquisition. Imperfect spoiling correction was completed using local scanner-sequence specific parameters (38).

Quantitative susceptibility mapping (QSM) maps were generated using the MPM data by applying the following pre-processing pipeline to PDw and T1w data: 3D complex phase data (adaptive combined using scanner software) were separated into odd and even echo trains and complex (non-linear) echo fitting (39) was applied to each train before unwrapping with a rapid

path-based minimum spanning tree algorithm (ROMEO) (40). Unwrapped (non-local) field maps were converted to Hz and averaged to create a single field-map. To increase QSM map accuracy, field maps were rotated to align the inferior-superior axis with the main direction of the scanner magnetic field, B0 (41). Separation of local from background field was completed using projection to dipole fields (PDF) (42), and brain masks for this step were generated by thresholding the phase quality maps generated during echo fitting. Dipole inversion was completed using STAR-QSM (43). Susceptibility maps created from T1w data were coregistered to their corresponding PDw space using SPM12 before both maps were averaged to give a final QSM map (44), (45).

qMRI region of interest extraction

Prior to structural processing, T1w MP2RAGE images were coregistered to their corresponding PDw MPM space using SPM12. Warped T1w images were then processed using the 'recon-all' pipeline with the 'highres' setting in Freesurfer version 7.1.0 (46). Errors in cortical surface reconstruction were manually corrected after visual inspection. The grey and white matter surfaces generated by Freesurfer were then used to define 12 equi-volume cortical depth volumes using LayNii (47), which were grouped together to produce the final 4 depth volumes [ref for this being a better method]. A version of the HCP-MMP1 atlas (48) projected onto fsaverage space (HCP-MMP1.0 projected on fsaverage) was then brought into each subject's native space using surface-based registration. Brodmann area 46 as defined in the HCP-MMP1 atlas was used as the DLPFC label, and this was transformed into a volumetric GM-SWM mask in PDw MPM space using Freesurfer. Using Matlab R2018a, the DLPFC was further divided into anterior, middle and posterior equi-volume sub-regions, before being intersected with the 4 GM depths and SWM masks to create 5 x 3 individual ROIs for each subject. Median QSM, R1, R2* and MTsat values were extracted from each of these ROIs using Matlab.

Spatial transcriptomics dataset description

Publicly available spatial transcriptomic data from postmortem dorsolateral prefrontal cortex was used for this analysis (22). Briefly, the sample set consists of 30 tissue blocks from 10 donors. For each donor, anterior, middle and posterior DLPFC samples were dissected and profiled. Brodmann area 46 was dissected in a plane perpendicular to the pial surface to capture cortical layers 1-6 and WM. The 10x Visium protocol was performed according to manufacturer's instructions on 10 um sections.Sequencing was performed on an Illumina NovaSeq 6000 with minimum depth of 50,000 reads per Visium spot.

Spatial transcriptomics layer partitioning

Data were used following processing previously described (22). Briefly, fastq and image data were pre-processed with the 10x SpaceRanger pipeline. Outputs from this step were processed in R, including filtration of undetected genes and spots with zero counts and QC metric assessment. This was followed by dimensionality reduction (n=50 PCs) and batch-correction using Harmony (49). Clustering was performed in a data-driven and spatially-aware manner using BayesSpace (50).

We opted to partition the spatial domains of the spatial transcriptomics data with a compromise of molecular feature and layer size compatible with the qMRI partitioning. To do this, we used BayesSpace clustering with n=7 clusters which partitioned the cortex into 5 spatial domains, of which cluster 1 consisted of a small endothelial-rich transcriptomic signature. Aware that this cluster would be included as part of SpD1 in the MRI data, we combined this cluster manually with cluster 2, resulting in 4 cortical spatial domains.

Gene ontology pathway selection

Existing literature predicts that qMRI metrics relate to specific biological processes. Keywords associated with these processes - namely, myelin, iron, mineral and lipids - were searched among gene ontology biological process pathways (https://geneontology.org/) (51). A list of pathways associated with these keywords was downloaded. Due to the hierarchical nature of GO pathways, we opted to also include all offspring pathways of our pathways of interest, since this could provide further insight into specific processes, for which we used the GO.db R package. This provided us with a list of all molecular pathways and their offspring we expected to be associated with entities captured in qMRI data. We then used the R package AnnotationDbi to fetch all gene symbols associated with each of the pathways of interest.

Spatial scoring of molecular pathways

In order to determine the level of expression of our pathways of interest, we adapted the scanpy (52) score_genes function to take in a custom gene background list. In brief, this function sums the expression of a list of genes of interest. It then subtracts from this score the summed expression of a list of randomly selected background genes of matching length. We made two modifications to this approach, firstly by allowing the use of a custom background gene list. This allowed us to use a gene ‘universe’ of genes captured in the data minus the genes of interest to avoid double-sampling. Secondly, following the subtraction of the background score, we divided our score by the sum of UMI in that spatial transcriptomics spot. This was done to account for layer-specific differences in UMI capture due to the differences in tissue permeabilisation in the white and grey matter, making scores more comparable across spatial domains regardless of myelination state.

Spatial transcriptomics layer-specific cell count estimation

The spatialDLPFC dataset was deconvoluted using cell2location (53) with paired single nuclear RNA sequencing data (22). This assigns to each spot a likelihood score of a given cell type being present within that spot. In order to ensure only the cell types we had the highest confidence of being present were counted, we considered the top 3 cell types with highest score to be present in a given spot.

Correlation analyses

qMRI metrics, cell count and GO pathway scores were adjusted for age and sex across ROIs using the covariance method (54). Mean, adjusted qMRI metrics, cell counts and GO pathway scores were calculated across subjects for each of the 5 x 3 ROIs. The Spearman correlation coefficients were then calculated for mean qMRI metrics versus mean cell counts, and mean

qMRI metrics versus mean GO pathway scores. Significant correlations were presented at FDR-corrected p<0.05 (55).

Prediction of control ST from qMRI data
Leave-one out cross validation (LOOCV) was completed by fitting a linear regression model to all but one ROI at a time like so: cell count or GO pathway score ~ QSM + R1 + R2* + MTsat + PrD. The cell count or GO pathway score for the left out region was predicted using the coefficients from the model and that region's qMRI metrics. The correlation between the predicted and actual cell count or GO pathway scores was assessed and significant correlations were assessed at FDR-corrected p<0.05.

Projection of PD ST scores from qMRI data
We built multivariate linear models across all 12 control ROIs like so: cell count or GO pathway score ~ QSM + R1 + R2* + MTsat + PrD. The coefficients from these models were used in combination with PD qMRI data to project PD cell counts and pathway score.

Cook's distance analysis of correlation robustness
For both qMRI vs ST and predicted vs actual LOOCV correlations, Cook's distance was calculated to assess the impact of individual data points on the overall correlation. We defined a threshold of 4/(N-k-1), where k is the number of explanatory variables and N is the number of observations (ROIs), above which individual points were considered to have a significant impact.

Parkinson's disease and control qMRI differences
Median qMRI metrics were extracted from the entire DLPFC at each cortical depth as well as SWM, and ANOVAs with the form *qMRI metric ~ age + sex + SpD*diagnosis* were fitted for each metric. Significant differences between PD and controls at a particular depth were assessed using the estimated marginal means (*emmeans*) package in R and presented at FDR-corrected *P*<0.05.

References

1. Bedard PL, Hyman DM, Davids MS, Siu LL. Small molecules, big impact: 20 years of targeted therapy in oncology. Lancet. 2020 Mar 28;395(10229):1078–88.
2. Zhong L, Li Y, Xiong L, Wang W, Wu M, Yuan T, et al. Small molecules in targeted cancer therapy: advances, challenges, and future perspectives. Signal Transduct Target Ther. 2021 May 31;6(1):201.
3. Song Y, Li J, Wu Y. Evolving understanding of autoimmune mechanisms and new therapeutic strategies of autoimmune disorders. Signal Transduct Target Ther. 2024 Oct 4;9(1):263.
4. Van Dyck CH, Swanson CJ, Aisen P, Bateman RJ, Chen C, Gee M, et al. Lecanemab in

early alzheimer's disease. N Engl J Med. 2023 Jan 5;388(1):9–21.

5. Miller TM, Cudkowicz ME, Genge A, Shaw PJ, Sobue G, Bucelli RC, et al. Trial of antisense oligonucleotide tofersen for SOD1 ALS. N Engl J Med. 2022 Sep 22;387(12):1099–110.
6. Seiler A, Nöth U, Hok P, Reiländer A, Maiworm M, Baudrexel S, et al. Multiparametric quantitative MRI in neurological diseases. Front Neurol. 2021 Mar 8;12:640239.
7. Leutritz T, Seif M, Helms G, Samson RS, Curt A, Freund P, et al. Multiparameter mapping of relaxation (R1, R2*), proton density and magnetization transfer saturation at 3 T: A multicenter dual-vendor reproducibility and repeatability study. Hum Brain Mapp. 2020 Oct 15;41(15):4232–47.
8. Vandeleene N, Guillemin C, Dauby S, Requier F, Charonitis M, Chylinski D, et al. Using quantitative magnetic resonance imaging to track cerebral alterations in multiple sclerosis brain: A longitudinal study. Brain Behav. 2023 May;13(5):e2923.
9. Johnson EB, Parker CS, Scahill RI, Gregory S, Papoutsi M, Zeun P, et al. Altered iron and myelin in premanifest Huntington's Disease more than 20 years before clinical onset: Evidence from the cross-sectional HD Young Adult Study. EBioMedicine. 2021 Mar 9;65:103266.
10. Rong J, Haider A, Jeppesen TE, Josephson L, Liang SH. Radiochemistry for positron emission tomography. Nat Commun. 2023 Jun 5;14(1):3257.
11. McAteer MA, McGowan DR, Cook GJR, Leung HY, Ng T, O'Connor JPB, et al. Translation of PET radiotracers for cancer imaging: recommendations from the National Cancer Imaging Translational Accelerator (NCITA) consensus meeting. BMC Med. 2025 Jan 23;23(1):37.
12. Hubbard Cristinacce PL, Keaveney S, Aboagye EO, Hall MG, Little RA, O'Connor JPB, et al. Clinical translation of quantitative magnetic resonance imaging biomarkers - An overview and gap analysis of current practice. Phys Med. 2022 Sep;101:165–82.
13. Lazari A, Lipp I. Can MRI measure myelin? Systematic review, qualitative assessment, and meta-analysis of studies validating microstructural imaging with myelin histology. Neuroimage. 2021 Apr 15;230:117744.
14. Cashmore MT, McCann AJ, Wastling SJ, McGrath C, Thornton J, Hall MG. Clinical quantitative MRI and the need for metrology. Br J Radiol. 2021 Apr 1;94(1120):20201215.
15. Stüber C, Morawski M, Schäfer A, Labadie C, Wähnert M, Leuze C, et al. Myelin and iron concentration in the human brain: a quantitative study of MRI contrast. Neuroimage. 2014 Jun;93 Pt 1:95–106.
16. Galbusera R, Bahn E, Weigel M, Schaedelin S, Franz J, Lu P-J, et al. Postmortem quantitative MRI disentangles histological lesion types in multiple sclerosis. Brain Pathol. 2023 Nov;33(6):e13136.
17. Duyn JH, Schenck J. Contributions to magnetic susceptibility of brain tissue. NMR Biomed. 2017 Apr;30(4).

18. Lutti A, Dick F, Sereno MI, Weiskopf N. Using high-resolution quantitative mapping of R1 as an index of cortical myelination. Neuroimage. 2014 Jun;93 Pt 2:176–88.

19. Hametner S, Endmayr V, Deistung A, Palmrich P, Prihoda M, Haimburger E, et al. The influence of brain iron and myelin on magnetic susceptibility and effective transverse relaxation - A biochemical and histological validation study. Neuroimage. 2018 Oct 1;179:117–33.

20. Helms G, Dathe H, Kallenberg K, Dechent P. High-resolution maps of magnetization transfer with inherent correction for RF inhomogeneity and T1 relaxation obtained from 3D FLASH MRI. Magn Reson Med. 2008 Dec;60(6):1396–407.

21. Weiskopf N, Suckling J, Williams G, Correia MM, Inkster B, Tait R, et al. Quantitative multi-parameter mapping of R1, PD(*), MT, and R2(*) at 3T: a multi-center validation. Front Neurosci. 2013 Jun 10;7:95.

22. Huuki-Myers LA, Spangler A, Eagles NJ, Montgomery KD, Kwon SH, Guo B, et al. A data-driven single-cell and spatial transcriptomic map of the human prefrontal cortex. Science. 2024 May 24;384(6698):eadh1938.

23. Hjelle N, Mohanty B, Hubbard T, Johnson MD, Wang J, Johnson LA, et al. Impairment of neuronal activity in the dorsolateral prefrontal cortex occurs early in parkinsonism. Front Neurosci. 2025 Jan 17;19:1521443.

24. Li H, Hu X, Gao Y, Cao L, Zhang L, Bu X, et al. Neural primacy of the dorsolateral prefrontal cortex in patients with obsessive-compulsive disorder. Neuroimage Clin. 2020 Sep 11;28:102432.

25. Kumar S, Zomorrodi R, Ghazala Z, Goodman MS, Blumberger DM, Cheam A, et al. Extent of dorsolateral prefrontal cortex plasticity and its association with working memory in patients with alzheimer disease. JAMA Psychiatry. 2017 Dec 1;74(12):1266–74.

26. Smucny J, Dienel SJ, Lewis DA, Carter CS. Mechanisms underlying dorsolateral prefrontal cortex contributions to cognitive dysfunction in schizophrenia. Neuropsychopharmacology. 2022 Jan;47(1):292–308.

27. Kirilina E, Helbling S, Morawski M, Pine K, Reimann K, Jankuhn S, et al. Superficial white matter imaging: Contrast mechanisms and whole-brain in vivo mapping. Sci Adv. 2020 Oct 7;6(41).

28. McColgan P, Helbling S, Vaculčiaková L, Pine K, Wagstyl K, Attar FM, et al. Relating quantitative 7T MRI across cortical depths to cytoarchitectonics, gene expression and connectomics: a framework for tracking neurodegenerative disease. BioRxiv. 2020 Feb 5;

29. Schirmer L, Velmeshev D, Holmqvist S, Kaufmann M, Werneburg S, Jung D, et al. Neuronal vulnerability and multilineage diversity in multiple sclerosis. Nature. 2019 Sep;573(7772):75–82.

30. Fairbrother-Browne A, Grant-Peters M, Brenton JW, Nelvagal H, Reynolds R, Lim YM, et al. Molecular and cellular signatures differentiate Parkinson’s disease from Parkinson’s disease with dementia. BioRxiv. 2025 Mar 4;

31. Lentferink DH, Jongsma JM, Werkman I, Baron W. Grey matter OPCs are less mature and less sensitive to IFNγ than white matter OPCs: consequences for remyelination. Sci Rep. 2018 Feb 1;8(1):2113.

32. Balbastre Y, Aghaeifar A, Corbin N, Brudfors M, Ashburner J, Callaghan MF. Correcting inter-scan motion artifacts in quantitative R1 mapping at 7T. Magn Reson Med. 2022 Jul;88(1):280–91.

33. Corbin N, Acosta-Cabronero J, Malik SJ, Callaghan MF. Robust 3D Bloch-Siegert based B1+ mapping using multi-echo general linear modeling. Magn Reson Med. 2019 Dec;82(6):2003–15.

34. Tabelow K, Balteau E, Ashburner J, Callaghan MF, Draganski B, Helms G, et al. hMRI - A toolbox for quantitative MRI in neuroscience and clinical research. Neuroimage. 2019 Jul 1;194:191–210.

35. Helms G, Dathe H, Dechent P. Quantitative FLASH MRI at 3T using a rational approximation of the Ernst equation. Magn Reson Med. 2008 Mar;59(3):667–72.

36. Edwards L, Pine K, Helms G, Weiskopf N. Rational approximation of the Ernst equation for dual angle R1 mapping revisited: Beyond the small flip-angle assumption. Book of Abstracts. Magn Reson Mater Phy; 2021. p. S45–6.

37. Weiskopf N, Callaghan MF, Josephs O, Lutti A, Mohammadi S. Estimating the apparent transverse relaxation time (R2(*)) from images with different contrasts (ESTATICS) reduces motion artifacts. Front Neurosci. 2014 Sep 10;8:278.

38. Corbin N, Callaghan MF. Imperfect spoiling in variable flip angle T1 mapping at 7T: Quantifying and minimizing impact. Magn Reson Med. 2021 Aug;86(2):693–708.

39. Liu T, Wisnieff C, Lou M, Chen W, Spincemaille P, Wang Y. Nonlinear formulation of the magnetic field to source relationship for robust quantitative susceptibility mapping. Magn Reson Med. 2013 Feb;69(2):467–76.

40. Dymerska B, Eckstein K, Bachrata B, Siow B, Trattnig S, Shmueli K, et al. Phase unwrapping with a rapid opensource minimum spanning tree algorithm (ROMEO). Magn Reson Med. 2021 Apr;85(4):2294–308.

41. Kiersnowski OC, Karsa A, Wastling SJ, Thornton JS, Shmueli K. Investigating the effect of oblique image acquisition on the accuracy of QSM and a robust tilt correction method. Magn Reson Med. 2023 May;89(5):1791–808.

42. Liu T, Khalidov I, de Rochefort L, Spincemaille P, Liu J, Tsiouris AJ, et al. A novel background field removal method for MRI using projection onto dipole fields (PDF). NMR Biomed. 2011 Nov;24(9):1129–36.

43. Wei H, Dibb R, Zhou Y, Sun Y, Xu J, Wang N, et al. Streaking artifact reduction for quantitative susceptibility mapping of sources with large dynamic range. NMR Biomed. 2015 Oct;28(10):1294–303.

44. Murdoch R, Kawadler J, Carmichael D, Kirkham F, Shmueli K. Can multi-parametric mapping sequences be used for accurate quantitative susceptibility mapping?

Proceedings of the International Society for Magnetic Resonance in Medicine. 2020;6.

45. Murdoch R. Developing MRI Quantitative Susceptibility Mapping to Investigate the Effect of Sickle Cell Anaemia on Brain Magnetic Susceptibility [Doctoral dissertation]. University College London; 2022.

46. Fischl B. Automatically parcellating the human cerebral cortex. Cereb Cortex. 2004 Jan 1;14(1):11–22.

47. Huber LR, Poser BA, Bandettini PA, Arora K, Wagstyl K, Cho S, et al. LayNii: A software suite for layer-fMRI. Neuroimage. 2021 Aug 15;237:118091.

48. Glasser MF, Coalson TS, Robinson EC, Hacker CD, Harwell J, Yacoub E, et al. A multi-modal parcellation of human cerebral cortex. Nature. 2016 Aug 11;536(7615):171–8.

49. Korsunsky I, Millard N, Fan J, Slowikowski K, Zhang F, Wei K, et al. Fast, sensitive and accurate integration of single-cell data with Harmony. Nat Methods. 2019 Dec;16(12):1289–96.

50. Zhao E, Stone MR, Ren X, Guenthoer J, Smythe KS, Pulliam T, et al. Spatial transcriptomics at subspot resolution with BayesSpace. Nat Biotechnol. 2021 Nov;39(11):1375–84.

51. Carbon S, Ireland A, Mungall CJ, Shu S, Marshall B, Lewis S, et al. AmiGO: online access to ontology and annotation data. Bioinformatics. 2009 Jan 15;25(2):288–9.

52. Wolf FA, Angerer P, Theis FJ. SCANPY: large-scale single-cell gene expression data analysis. Genome Biol. 2018 Feb 6;19(1):15.

53. Kleshchevnikov V, Shmatko A, Dann E, Aivazidis A, King HW, Li T, et al. Cell2location maps fine-grained cell types in spatial transcriptomics. Nat Biotechnol. 2022 May;40(5):661–71.

54. Jack CR, Twomey CK, Zinsmeister AR, Sharbrough FW, Petersen RC, Cascino GD. Anterior temporal lobes and hippocampal formations: normative volumetric measurements from MR images in young adults. Radiology. 1989 Aug;172(2):549–54.

55. Benjamini Y, Hochberg Y. Controlling the false discovery rate: a practical and powerful approach to multiple testing. Journal of the Royal Statistical Society: Series B (Methodological). 1995 Jan;57(1):289–300.

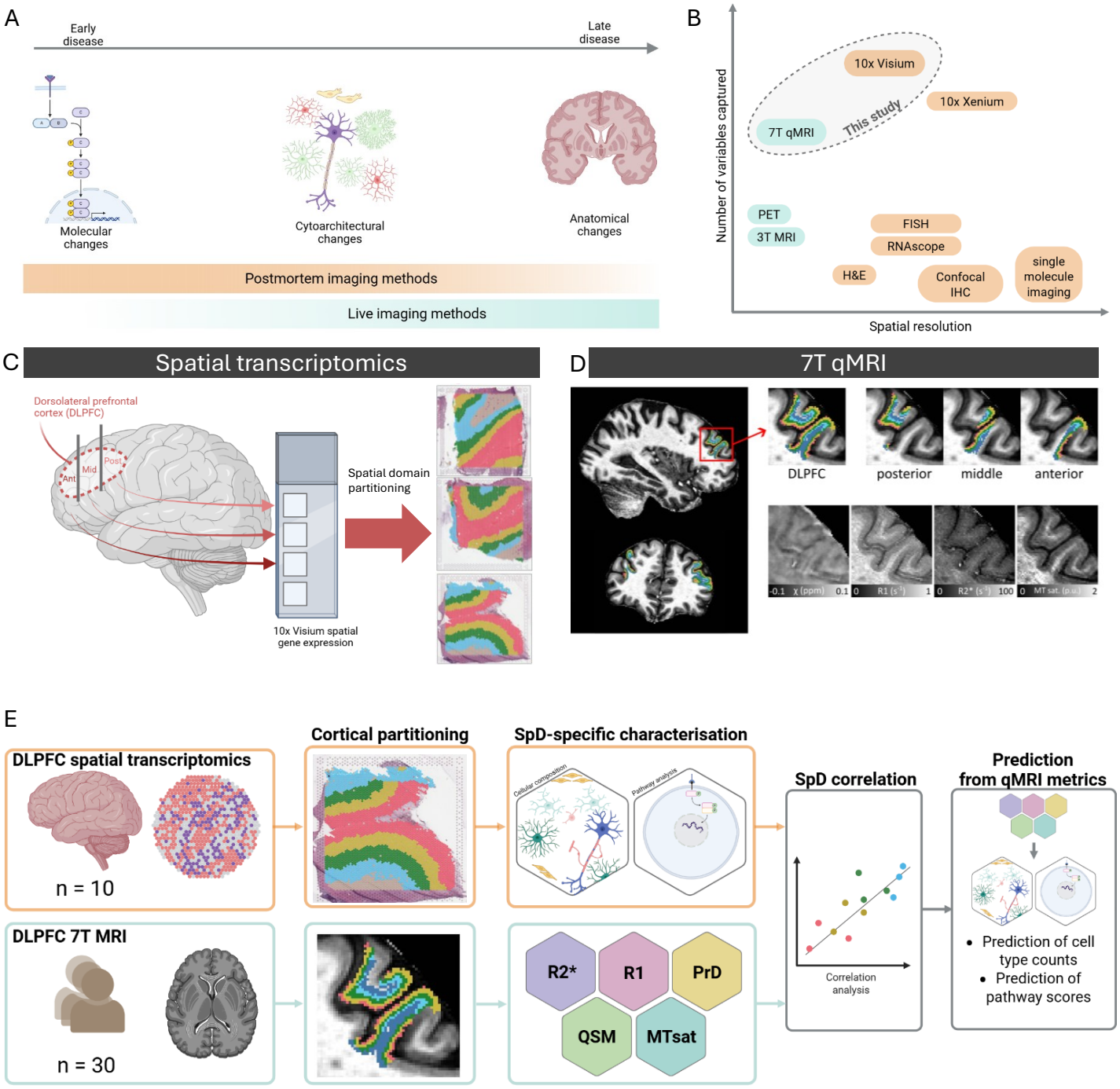

Figure 1 Integration of ultra-high resolution qMRI and spatial transcriptomics (A) MRI technologies can capture non-invasively disease features in live patients, however by the time disease features are detectable anatomically, irreversible cellular and molecular damage has already occurred. In contrast, spatial transcriptomics methods can capture molecular and cellular features which might be present in early disease, but are generally employed in postmortem samples. (B) Recent advances in both qMRI and ST mean the resolution and number of variables captured by these variables make integration of these methods possible for the first time. (C) Diagram of sample structure of the DLPFC. Samples were dissected to include anterior, middle and posterior DLPFC. Grey matter of each section was partitioned into 4 spatial domains. (D) Diagram of sample structure of 7T qMRI data. DLPFC was selected according to region selection of ST data and grey matter cortex was partitioned into 4 spatial domains. (E) Study design diagram. We used ST data to calculate estimates of cellular composition and expression of biological pathways in each ROI. We characterized the relationship of these metrics in relation to qMRI metrics from these ROIs in 7T qMRI. We then created models to predict the molecular and cellular information from qMRI data.

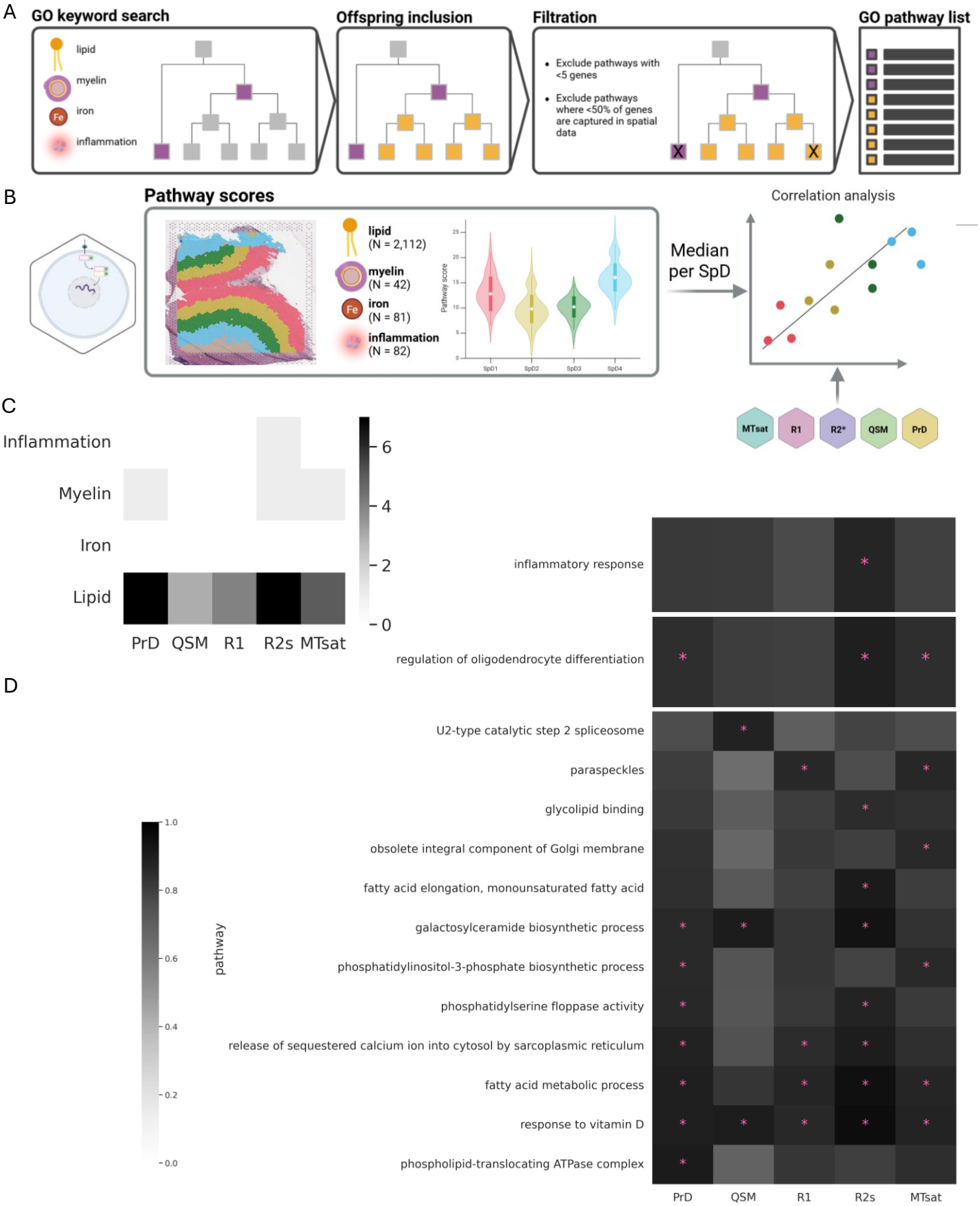

Figure 2 Characterising linear relationships between biological pathways and qMRI metrics (A) Schematic of GO biological process pathway selection. All pathways containing selected keywords (lipid, myelin, iron, inflammation) and their offspring were included. All pathways which did not have at least 5 genes or which ST data did not detect at least 50% of genes were excluded. (B) Pathway expression scores were calculated and correlative relationships with qMRI metrics were characterized. (C) Heatmap showing how many pathways in each category significantly correlated with qMRI metrics. Lipid pathways correlated most frequently with qMRI metrics. Heatmap showing correlation R2 (colour) and significance of correlation (*).

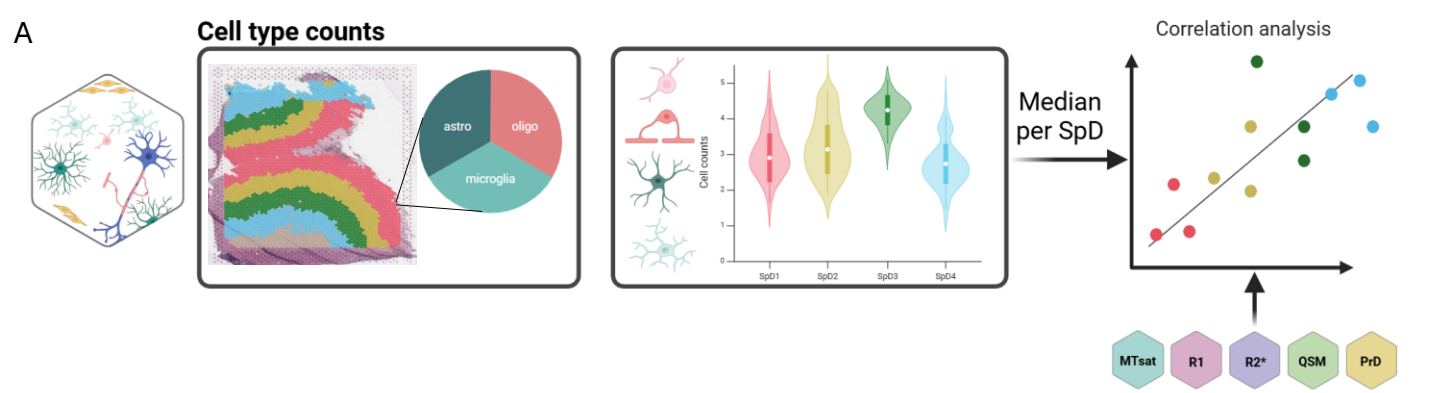

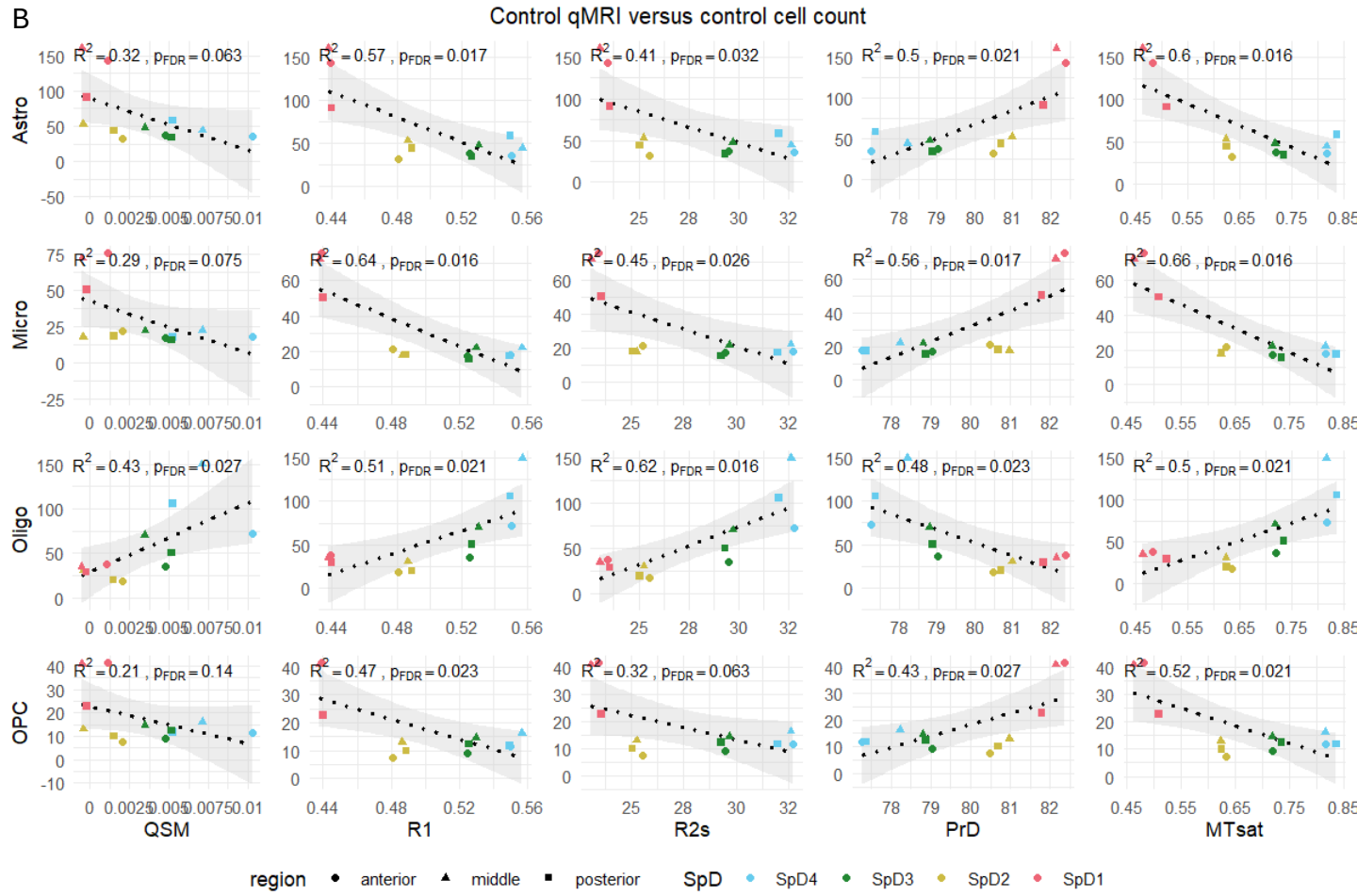

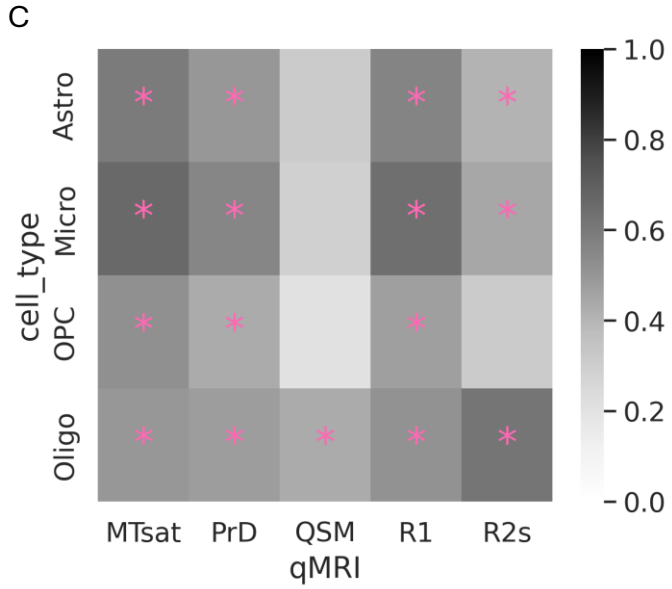

Figure 3 Characterising linear relationships between cell type proportions and qMRI metrics (A) Schematic of cell type count data acquisition. Spatial transcriptomic data was deconvoluted using cell2location. Cell types with top 3 cell2location scores were counted as present in a given spot, the median cell count per ROI was then correlated to the median qMRI metrics per ROI. (B) Correlative analysis of cell counts in relation to qMRI metrics. Oligodendrocytes had the most significant correlations with qMRI metrics and most even distribution of ROIs. (C) Heatmap summarizing correlation relationships of cell counts in relation to qMRI metrics. The correlation R2 (colour) and significance of correlation (*).

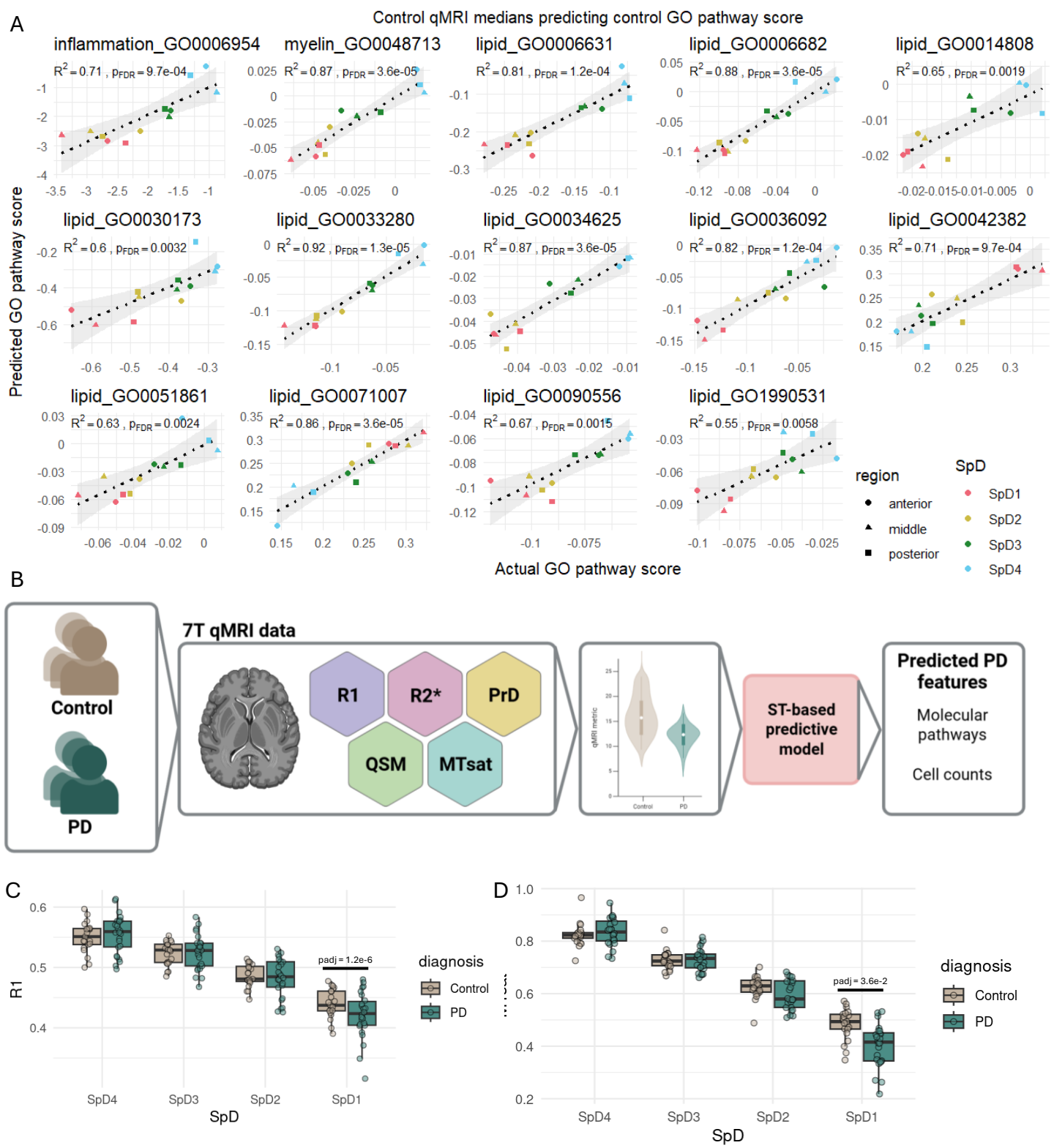

Figure 4 Prediction of molecular metrics from qMRI data using ST-based models (A) Results of leave-one-out analysis predicting biological pathways from qMRI data. All pathways that had at least one significant linear relationship with a qMRI metric could be significantly predicted from qMRI data. (B) Schematic illustrating disease application of predictive model. We leveraged the model constructed with the leave-one-out analysis and predicted the molecular features of qMRI data from Parkinson's disease patients. (C) qMRI data from PD patients had significantly lower Mtsat and R1 in control SpD1.

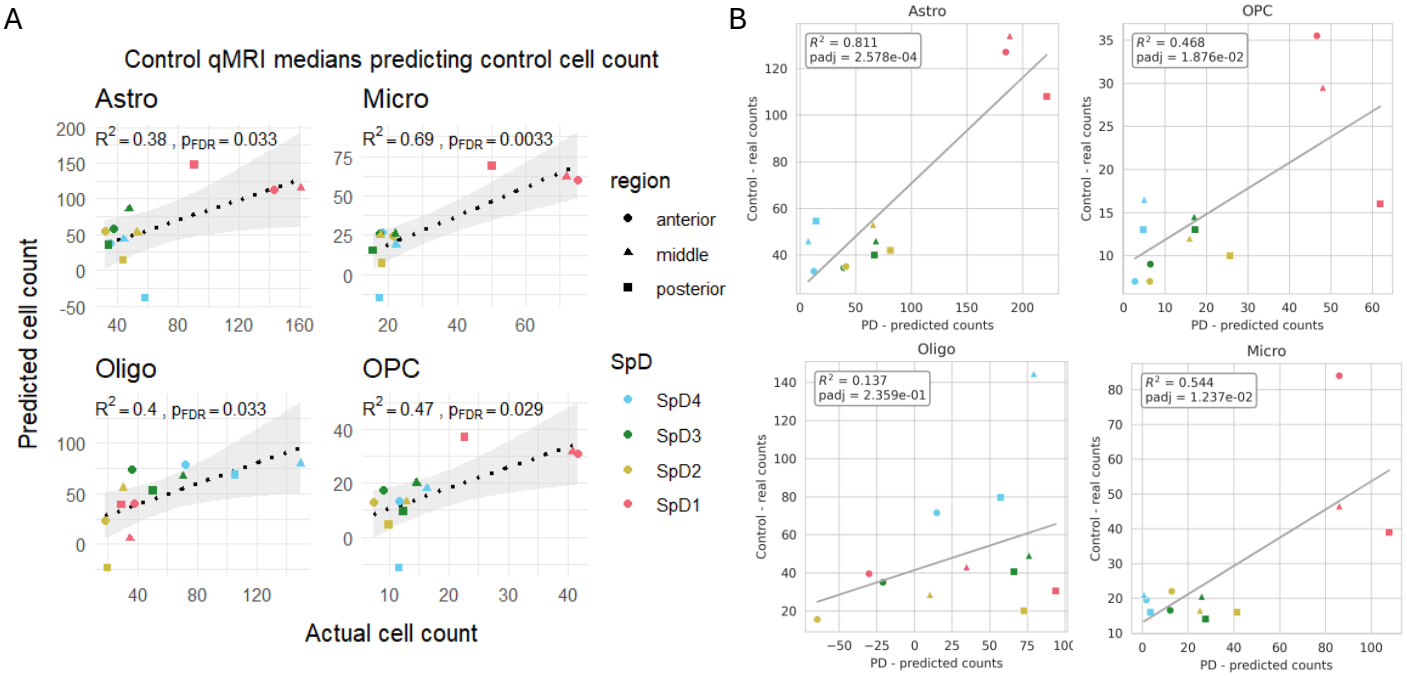

Figure 5 Predicting cell counts in PD from qMRI data (A) Results of leave-one-out analysis predicting cell counts from qMRI data. All tested glial cell types could be significantly predicted from qMRI data. (B) We predicted cell counts in PD and characterized their correlative relationship with control real counts from ST. Astrocytes, microglia and OPCs had significant correlations with control data, suggesting no change in these cell types was detectable. Oligodendrocytes had multiple predictions of negative cell counts (suggesting cell counts lower than training ST data) and a loss of correlation, suggesting a change in oligodendrocyte distribution across spatial domains.